Host Structure Engineering in Thermoelectric Clathrates

M. Christensen and B. B. Iversen*

Department of Chemistry, University of Aarhus, DK-8000 Aarhus C, Denmark

Received May 27, 2007. Revised Manuscript Received July 9, 2007

Three $Ba_8Al_{16}Ge_{30}$ clathrate type I samples have been prepared using three different synthesis methods; flux growth, Czochralski growth, and stoichiometric mixing. The samples were characterized by X-ray powder diffraction, multi-temperature single-crystal X-ray diffraction, high-resolution low-temperature (20 K) single-crystal neutron diffraction, and measurement of transport properties. The samples show a remarkable variation in the aluminum/germanium occupancies on the host-structure sites and minor variation in the total aluminum content. The observed occupancy variation forms the basis for the formulation of a set of simple rules for the maximum site occupancy factors of trivalent elements in the host structure. The rules provide an explanation for why the overwhelming majority of clathrate samples containing trivalent elements are *n*-type rather than *p*-type. The nuclear density of the barium guest atom in the large cage is calculated from the neutron diffraction data, and it is found to be strongly dependent on the host structure and the exact aluminum siting. Thus, the sample with low aluminum content has a prolate-shaped barium nuclear density, whereas a higher aluminum content leads to the well-known torus shape observed in other clathrates. This demonstrates that the host−guest interactions are not merely ionic and that they significantly influence the guest-atom structure and dynamics. Comparison of derived Einstein temperatures and bond distances for the three samples reveals that the compound with the highest aluminum content (flux growth) has the strongest host−guest interaction, even though it also has the largest unit cell. Again, the specific properties of the guest atoms are not only determined by the clathrate cage size but also by the subtle chemical interactions between the host structure and the guest. The thermal conductivity is about 3 times smaller for the stoichiometric sample than for the Czochralski-pulled sample. Thus, control of the host-structure chemistry is not only a key to manipulating the electrical properties of clathrates but also the thermal conductivity.

Introduction

Host−guest structures offer an interesting area of research because their physical properties can be engineered through chemical changes of either the guest or the host. In thermoelectric research, host−guest structures of skutterudites and clathrates have been intensively investigated, because they the fulfill the design concept of a "Phonon glass−electron crystal" (PGEC).[1] The general assumption is that loosely bound guest atoms provide a scattering mechanism for the acoustic phonons, thereby satisfying the "phonon glass" part of the concept. The "electron crystal" part, on the other hand, is associated with the host structure, and it can be optimized through atomic substitution. The thermoelectric efficiency of a material is governed by the figure of merit (zT), which is a dimensionless quantity, $zT = TS^2\sigma/\kappa$. Here, T is the temperature, S is the Seebeck coefficient, and σ and κ are the electrical and thermal conductivity, respectively.

The intense interest in clathrates has been triggered by a number of unique properties.[2−8] The clathrates have extreme chemical resistance, high-temperature stability, low thermal conductivity, and excellent chemical tunability through variation of either the host structure or the guest atom. The host structure can accommodate atoms in different valence states, and varying their ratio allows tuning of the electrical properties. For the $Ba_8Ga_{16+x}Ge_{30-x}$ system, this leads to *p*-type properties for $x > 0$ and *n*-type properties for $x < 0$. The archetypical clathrate, $Ba_8Ga_{16}Ge_{30}$, indeed has excellent thermoelectric properties at high temperature, with zT reaching 1.35 at 900 K.[9,10]

The primary guideline for understanding clathrate compounds has been the Zintl concept. In this picture, four electrons must be available for each tetradrahedrally bonded host atom. The guest atom is assumed to be ionic and

* To whom correspondence should be addressed. E-mail: bo@chem.au.dk.

(1) Slack, G. A. In *New Materials and Performance Limits for Thermoeletric Cooling*; Rowe, D. M., Ed.; CRC Press: Boca Raton, FL, 1995.
(2) Nolas, G. S.; Cohn, J. L.; Slack, G. A.; Schujman, S. B. *Appl. Phys. Lett.* **1998**, *73*, 3133−3144.
(3) Sales, B. C.; Chakoumakos, B. C.; Jin, R.; Thompson, J. R.; Mandrus, D. *Phys. Rev. B* **2001**, *63*, 245113.
(4) Paschen, S.; Pacheco, V.; Bentien, A.; Sanchez, A.; Carrillo-Cabrera, W.; Baenitz, M.; Iversen, B. B.; Grin, Y.; Steglich, F. *Physica B* **2003**, *328*, 39−43.
(5) Bentien, A.; Christensen, M.; Bryan, J. D.; Sanchez, A.; Paschen, S.; Steglich, F.; Stucky, G. D.; Iversen, B. B. *Phys. Rev. B* **2004**, *69*, 045107.
(6) Umeo, K.; Avila, M. A.; Sakata, T.; Suekuni, K.; Takabatake, T. *J. Phys. Soc. Jpn.* **2005**, *74*, 2145−2148.
(7) Hermann, R. P.; Keppens, V.; Bonville, P.; Nolas, G. S.; Grandjean, F.; Long, G. J.; Christen, H. M.; Chakoumakos, B. C.; Sales, B. C.; Mandrus, D. *Phys. Rev. Lett.* **2006**, *97*, 017401.
(8) Christensen, M.; Lock, N.; Overgaard, J.; Iversen, B. B. *J. Am. Chem. Soc.* **2006**, *128*, 15657−15665.
(9) Saramat, A.; Svensson, G.; Palmqvist, A. E. C.; Stiewe, C.; Mueller, E.; Platzek, D.; Williams, S. G. K.; Rowe, D. M.; Bryan, J. D.; Stucky, G. D. *J. Appl. Phys.* **2006**, *99*, 023708.
(10) Christensen, M.; Snyder, G. J.; Iversen, B. B. *Proc. 25th Int. Conf. on Thermoelectrics* **2006**.

10.1021/cm071435p CCC: $37.00
Published on Web 09/05/2007

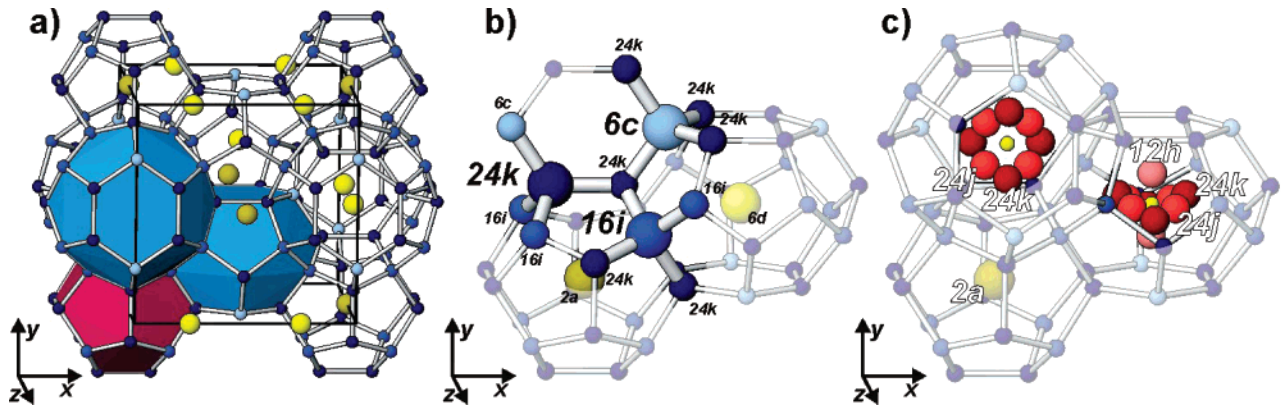

Figure 1. Crystal structure of the type I clathrate. The yellow atoms denote the guest atoms with the light-yellow being the 6*d* position and the dark-yellow the 2*a* position. The host structure is also shown with varying color intensity: the 6*c* (light-blue), 16*i* (medium-blue), and 24*k* (dark-blue). Part a) shows the unit cell with the large tetradecahedral cage in light-blue and the dodecahedral cage in dark-red; b) shows the bonding arrangement of the different sites, where the atoms' sizes are intended to enhance the clarity; in c) the different guest atoms' sites in the large cage are illustrated: 12*h* (light-red), 24*j* (medium-red), and 24*k* (dark-red).

assumed to donate its valence electrons to the host structure, although in case of the inverse clathrates, the guest atom accepts electrons. Thus, in $Ba_8Ga_{16}Ge_{30}$, each of the eight barium guest atoms donates two electrons to the host structure, giving a total of 16 transferred electrons. The valences of the 16 gallium and 30 germanium atoms in the host structure are three and four, respectively. This gives a total of 184 valence electrons available for covalent bonding between the 46 host-structure atoms, and the compound is expected to be a semiconductor. The Zintl model forms the basis for the commonly held belief that the host−guest interactions are purely ionic and simply a function of the relative cage size available for the cation.

Most clathrate compositions form cubic structures belonging to space group *Pm*-3*n*. The structure is shown in part a of Figure 1, where polyhedra are used to visualize the two different cages. Three different crystallographic sites form the host structure 6*c*, 16*i*, and 24*k*. Part b of Figure 1 shows the atomic arrangement around the individual sites. The guest atom at the center of the small cage (2*a*) is denoted as Ba1, and the guest atom in the vicinity of the center of the large cage (6*d*) is referred to as Ba2. The possible sites around the center of the large cage are shown in part c of Figure 1, and they are denoted as 12*h*, 24*j*, and 24*k*. The majority of the studies in the literature have focused on the position, substitution, and dynamics of the guest atom in structures such as $X_8Ga_{16}Ge_{30}$ (X = Eu, Sr, and Ba).[3,11−15] The host structure has attracted much less attention, which is partly due to the crystallographic challenge presented by the weak scattering contrast between gallium/germanium for both X-rays and neutrons. Some studies have suggested that the host-structure sites are randomly occupied by group III and IV atoms.[3,14,15] However, early on, a maximum entropy method (MEM) analysis of X-ray diffraction data on $Sr_8Ga_{16}Ge_{30}$ and $Ba_8Ga_{16}Ge_{30}$ actually found a preference for gallium at the 6*c* site and depletion of gallium at the 16*i* site.[16] This result is supported by investigations of compounds with higher scattering contrast.[17,18] Resonance X-ray powder diffraction at the gallium absorption edge in $Sr_8Ga_{16}Ge_{30}$ later confirmed the MEM results; however, quantitative assessments of host-structure occupancies proved difficult.[19,20] Recently, quantitative assessments of the host-structure occupancies were reported for $Ba_8Ga_{16}Ge_{30}$ on the basis of single-crystal synchrotron resonance X-ray diffraction data.[8] It was found that the synthesis method influenced the gallium occupancy at the 6*c* site, and, furthermore, the guest-atom position and dynamics also appeared to be influenced by the host-structure occupancy. The host-structure occupancies therefor appear not only to provide an additional handle for optimizing the electrical properties, but they also control the chemical interactions with the guest atom. The strength of this interaction, that is, the coupling, affects how strongly a given guest atom can scatter phonons, and thus it affects the thermal conductivity of the compound. In other words, it is the chemistry of the clathrates, which underlies their much studied physical properties, and attention therefore must be directed toward this aspect. Here, we attempt to understand in detail the host-structure chemistry.

In the present study, control of the host-structure occupancy in $Ba_8Al_{16}Ge_{30}$ is achieved by varying the synthesis method. Substitution of gallium with aluminum provides good elemental contrast in X-ray and neutron diffraction experiments. Three different samples have been synthesized, and significant differences in the aluminum/germanium distribution were observed, depending on synthesis conditions. The observed occupancies are explained with the

(11) Paschen, S.; Carrillo-Cabrera, W.; Bentien, A.; Tran, V. H.; Baenitz, M.; Grin, Y.; Steglich, F. *Phys. Rev. B* **2001**, *64*, 214404.
(12) Qiu, L.; Swainson, I. P.; Nolas, G. S.; White, M. A. *Phys. Rev. B* **2004**, *70*, 035208.
(13) Baumbach, R.; Bridges, F.; Downward, L.; Cao, D.; Chesler, P.; Sales, B. *Phys. Rev. B* **2005**, *71*, 024202.
(14) Chakoumakos, B. C.; Sales, B. C.; Mandrus, D. G. *J. Alloys and Compounds* **2001**, *322*, 127−134.
(15) Chakoumakos, B. C.; Sales, B. C.; Mandrus, D. G.; Nolas, G. S. *J. Alloys Compd.* **2000**, *296*, 80−86.
(16) Bentien, A.; AEC, A. E. C. P.; Bryan, J. D.; Latturner, S.; Stucky, G. D.; L, L. F.; Iversen, B. B. *Angew. Chem., Int. Ed.* **2000**, *39*, 3613−3616.
(17) Eisenmann, B.; Schäfer, H.; Zagler, R. *J Less-Com. Met.* **1986**, *118*, 43−55.
(18) Bentien, A.; Nishibori, E.; Paschen, S.; Iversen, B. B. *Phys. Rev. B* **2005**, *71*, 144107.
(19) Zhang, Y. G.; Lee, P. L.; Nolas, G. S.; Wilkinson, A. P. *Appl. Phys. Lett.* **2002**, *80*, 2931−2933.
(20) Zhang, Y.; Wilkinson, A. P.; Nolas, G. S.; Lee, P. L.; Hodges, J. P. *J. Appl. Crystallogr.* **2003**, *36*, 1182−1189.

Table 1. Site Occupancy Factor of Aluminum at the Three Different Host Structure Sites (in %) Obtained for the Three Different Samples[a]

	Czo X−ray powder	Czo X−ray single	Czo Neutron single	norm X−ray powder	norm X−ray single	norm neutron single	flux X−ray powder	flux X−ray single
6*c*(Al)%	89(1)	97.4(6)	96(1)	67(1)	66.2(4)	67(1)	55(2)	55.8(2)
16*i*(Al)%	36(1)	43.5(4)	43(1)	27(1)	30.0(6)	31(1)	16(1)	24.0(5)
24*k*(Al)%	0.2(1.0)	5.2(2)	9(1)	28(1)	29.6(3)	27(1)	36(1)	39.5(5)
Al atoms	11.4(4)	14.0(1)	14.8(2)	15.1(4)	15.9(2)	15.5(2)	14.3(4)	16.7(1)
Ge atoms	34.6(4)	32.0(1)	31.2(2)	30.9(4)	30.1(2)	30.5(2)	31.7(4)	29.3(1)
6*c* + 24*k*(Al)%	91(2)	103(1)	105(1)	96(2)	96(1)	94(1)	91(2)	95(1)
16*i* + 24*k*(Al)%	37(2)	49(1)	52(1)	55(2)	60(1)	58(1)	51(2)	64(1)

[a] Aluminum and germanium contents per unit cell are also listed as well as summed sof's for 6*c* + 24*k* and 16*i* + 24*k*.

introduction of simple rules for the site occupancy factor (sof). Additionally, high-resolution single-crystal neutron diffraction data measured at 20 K provide detailed nuclear density maps of the guest atoms. The data expose a correlation between the host-structure occupancy and the Ba2 guest-atom disorder.

Experimental Section

Synthesis. The three samples used in this study were prepared in three different ways; Czochralski pulling, conventional stoichiometric mixing, and self-flux growth. The samples will be referred to as $Ba_8Al_{16}Ge_{30}$_czo, $Ba_8Al_{16}Ge_{30}$_norm, and $Ba_8Al_{16}Ge_{30}$_flux. The synthesis procedures for the stoichiometric and the self-flux-grown samples of $Ba_8Al_{16}Ge_{30}$ are similar to those used for $Ba_8Ga_{16}Ge_{30}$ using aluminum as flux instead of gallium.[8] The $Ba_8Al_{16}Ge_{30}$_czo sample was pulled from a melt consisting of a precursor Ba_6Ge_{25} and the pure elements of barium and aluminum with the total stoichiometry of Ba/Al/Ge being equal to 8:16:30. An induction furnace was used for the Czochralski pulling. The furnace chamber was purged and filled with helium gas to a pressure of 100 PSI to provide an inert atmosphere. The sample was pulled at a speed of 4 mm/hour. The various synthesis conditions give a significant difference in the thermal histories experienced by the samples.

Powder Diffraction. Powder diffraction data was measured in reflection geometry using a Bruker D8 Advance equipped with a curved Johansson germanium monochromator (Cu Kα1) and an energy dispersive Sol-X detector. The powder samples were attached to the surface of an oblique cut silicon single crystal using ethanol. LaB_6 was added as an internal standard. The program *Fullprof* was used to carry out Rietveld refinements, and these yielded estimates of the unit cell parameters and the germanium/aluminum occupancy at the individual host-structure sites.[21] The unit cell is observed to expand from $Ba_8Al_{16}Ge_{30}$_czo (a_{czo} = 10.83863(3) Å) to $Ba_8Al_{16}Ge_{30}$_norm (a_{norm} = 10.84865(6) Å) and even further to $Ba_8Al_{16}Ge_{30}$_flux (a_{flux} = 10.85334(3) Å). The $Ba_8Al_{16}Ge_{30}$ structure surprisingly has a larger unit cell (0.05−0.1 Å) than the corresponding gallium system ($Ba_8Ga_{16}Ge_{30}$). One would expect that the smaller size of Al^{3+} compared with Ga^{3+} would lead to the opposite result.[22] For the three $Ba_8Al_{16}Ge_{30}$ samples studied here, the unit cell increases with increasing aluminum content. The refined occupancies are listed in Table 1, where they are compared to the occupancies extracted from the single-crystal diffraction experiments. The barium guest atom in the large cage was modeled with anisotropic atomic displacement parameters (ADPs), whereas the host-structure atoms were constrained to have identical isotropic ADPs to limit correlation with the sof's. Selected experimental details are given in part a of Table 2, and full details are deposited in the Supporting Information.

Table 2. Selected Crystallographic Information from the Powder Diffraction Refinements[a]

298 K	$Ba_8Al_{16}Ge_{30}$ czo	$Ba_8Al_{16}Ge_{30}$ norm	$Ba_8Al_{16}Ge_{30}$ flux
model	6d	6d	6d
unit cell (Å)	10.83863(3)	10.84865(5)	10.85335(3)
B_{iso}(Ba1, host)	1.0(1)	0.9(1)	0.9(1)
B_{iso}(Ba2)	2.2(1)	2.6(1)	3.4(1)
x(Ge2)	0.1842(2)	0.1844(2)	0.1843(2)
y(Ge3)	0.3072(2)	0.3065(3)	0.3089(4)
z(Ge3)	0.1158(2)	0.1155(3)	0.1175(3)
# params	33	31	40
$\sin\theta/\lambda$ (Å^{-1})	0.42	0.44	0.53
N_{ref} ph1/ph2/ph3	85/12	99/13	168/20/12
observations	4295	4564	6289
R_p/R_{wp}	14.5/17.8	22.4/26.8	20.5/26.0
R_{exp}/χ^2	13.4/1.7	17.5/2.3	20.2/1.7
R_F/R_I $Ba_8Al_{16}Ge_{30}$_x	5.4/8.1	8.9/12.3	7.5/8.2
R_F/R_I LaB_6	3.1/7.8	4.2/7.4	3.1/4.8
R_F/R_I Ge			7.7/14.2

[a] The refinements used the following coordinates: Ba1 *2a*(0,0,0), Ba2 *6d*(1/4,1/2,0), Al1/Ge1 *6c*(1/4,0,1/2), Al2/Ge2 *16c*(*x*,*x*,*x*), and Al3/Ge3 *24k*(0,*y*,*z*).

Single-Crystal X-ray Diffraction. Conventional multi-temperature X-ray diffraction data were measured on a Bruker APEX-II diffractometer equipped with a Mo Kα source. An Oxford liquid nitrogen cryostream provided temperature control, and full data sets were collected at 100, 200, 300, and 400 K. Relatively small crystals were used for the measurements to minimize absorption and extinction effects. Table 3 lists experimental and crystallographic details. The data were integrated using *SAINT*+, and empirical absorption correction and averaging was performed using *SADABS*. The structural refinements were done with the program *SHELX*.[23] The host-structure sites were constrained to be fully occupied. The data were refined against five different models with respect to the barium guest-atom siting in the large cage. The following shorthand notation will be used for the different models: Ba2 at the 6*d* position with anisotropic ADPs, "Ba6*d*"; Ba2 at the 24*j* position with isotropic ADPs, "Ba24*j*"; Ba2 at the 24*k* position with isotropic ADPs, "Ba24*k*"; Ba2 at the 24*j* position with anisotropic ADPs, "Ba24*j_aniso*"; Ba2 at the 24*k* position with anisotropic ADPs, "Ba24*k_aniso*". The Ba24*k_aniso* model showed the overall best agreement factors, although the agreement factors are almost indistinguishable between the different models (Supporting Information). However, the Ba24*k_aniso* model also contains the largest number of refined parameters, and it shows large correlation between positional parameters and ADPs for the Ba2 guest atom. The results from the Ba6*d* and Ba24*k* models are discussed below, because these models do not have strong correlations between parameters.

Single-Crystal Neutron Diffraction. A sample obtained from the conventional stoichiometric synthesis and a sample cut from

(21) Rodriguez-Carvajal, J. *Fullprof*, ver. 3.20; Feb 2005.
(22) *Handbook of Chemistry and Physics*, 77th ed.; Lide, D. R., Ed.; CRC Press: Boca Raton, FL, 1996−1997.
(23) Sheldrick, G. M. *SAINT-Plus*, *SADABS*, and *SHELX* programs; Bruker AXS Inc.: Madison, WI, 2003.

Table 3. Diffraction Refinements Given for the Three Different Samples in the Ba6d and Ba24k Models[a]

300 K	$Ba_8Al_{16}Ge_{30}$_czo		$Ba_8Al_{16}Ge_{30}$_norm		$Ba_8Al_{16}Ge_{30}$_flux	
unit cell (Å)	10.8402(1)		10.8513(2)		10.8533(1)	
vol (μm^3)	80 × 80 × 80		50 × 70 × 80		80 × 100 × 100	
μ (mm^{-1})	24.85		23.66		23.08	
sin θ/λ ($Å^{-1}$)	1.02		1.10		1.00	
$N_{integrated}$	14 033		23 443		12 468	
N, $N(F > 4\sigma(F))$	1061, 761		1307, 799		996, 707	
model	Ba6d	Ba24k	Ba6d	Ba24k	Ba6d	Ba24k
U_{iso}(Ba1) ($10^{-4}Å^2$)	103(1)	100(1)	118(2)	113(2)	122(1)	113(2)
x(Ba2)	1/4	0.2490(3)	1/4	0.2489(3)	1/4	0.2491(2)
z(Ba2)	0	0.0155(1)	0	0.0214(1)	0	0.0246(1)
U_{11}(Ba2) ($10^{-4}Å^2$)	175(2)		179(3)		160(3)	
U_{22}(Ba2) ($10^{-4}Å^2$)	343(2)		565(4)		698(4)	
U_{iso}(Ba2) ($10^{-4}Å^2$)	287(2)	178(2)	436(4)	204(3)	519(4)	199(3)
x(Ge2)	0.18451(3)	0.18450(3)	0.18459(3)	0.18459(4)	0.18452(3)	0.18452(3)
y(Ge3)	0.30764(3)	0.30764(3)	0.30846(5)	0.30846(5)	0.30897(5)	0.30899(5)
z(Ge3)	0.11669(3)	0.11669(3)	0.11635(5)	0.11634(6)	0.1162(5)	0.11623(5)
U_{iso}(host) ($10^{-4}Å^2$)	96.6(1)	96.3(1)	109.2(2)	109.8(2)	110.5(1)	110.1(2)
N_{par}, $N_{constrains}$	22, 3	23, 3	22,3	23,3	22,3	23, 3
R_F, $R_F(F > 4\sigma(F))$	3.74, 2.34	3.79, 2.38	8.40, 3.86	8.97, 4.38	5.53, 3.28	6.39, 3.82
GOF, R_{wl} (N)	0.55, 8.41	0.56, 8.55	0.88, 15.13	0.96, 16.45	1.00, 6.11	1.19, 7.14

[a] The refinements used the following coordinates: Ba1 *2a*(0,0,0), Ba2 *6d*(1/4,1/2,0) or *24k*(*x*,1/2,*z*), Al1/Ge1 *6c*(1/4,0,1/2), Al2/Ge2 *16c*(*x*,*x*,*x*), and Al3/Ge3 *24k*(0,*y*,*z*).

Table 4. Selected Crystallographic Information from the Neutron Diffraction Refinements. The Refined Values Are Given for 6d and 24k Model for the Czochralski Pulled and Conventionally Synthesized Sample[a]

20 K	$Ba_8Al_{16}Ge_{30}$_czo		$Ba_8Al_{16}Ge_{30}$_norm	
unit cell (Å)	10.803(2)		10.810(2)	
mass (mg)	47.3		109.4	
sin θ/λ ($Å^{-1}$)	1.48		1.60	
N_{ref}, $N_{ref}(I > 3\sigma(I))$	14 478, 6125		19 605, 7421	
Model	Ba6d	Ba24k	Ba6d	Ba24k
U_{iso}(Ba1) ($10^{-4}Å^2$)	40(2)	40(2)	25(2)	21(2)
x(Ba2)	1/4	0.2477(13)	1/4	0.2496(5)
z(Ba2)	0	0.0082(8)	0	0.0174(2)
U_{11}(Ba2) ($10^{-4}Å^2$)	71(4)		47(4)	
U_{22}(Ba2) ($10^{-4}Å^2$)	106(3)		292(6)	
U_{iso}(Ba2) ($10^{-4}Å^2$)	94(2)	65(8)	211(4)	61(4)
x(Ge2)	0.18439(3)	0.18439(3)	0.18440(2)	0.18440(2)
y(Ge3)	0.30774(3)	0.30774(3)	0.30844(3)	0.30845(3)
z(Ge3)	0.11654(3)	0.11654(3)	0.11639(3)	0.11639(3)
U_{iso}(host) ($10^{-4}Å^2$)	43.6(4)	27.0(2)	35.9(3)	22.2(2)
N_{par}, $N_{constrains}$	45, 4	46, 4	41, 4	42, 4
R_F, $R_F(I > 3\sigma(I))$	27.8, 13.3	27.8, 13.3	32.9, 13.5	32.8, 13.5
R_{wF}, $R_{wF}(I > 3\sigma(I))$	9.8, 7.3	9.8, 7.3	13.1, 9.0	13.1, 9.0
R_{wI}, $R_{wI}(I > 3\sigma(I))$	16.2, 12.8	16.2, 12.8	20.8, 14.8	20.8, 14.8

[a] The refinement used the following coordinates: Ba1 *2a*(0,0,0), Ba2 *6d*(1/4,1/2,0) or *24k*(*x*,1/2,*z*), Al1/Ge1 *6c*(1/4,0,1/2), Al2/Ge2 *16c*(*x*,*x*,*x*), and Al3/Ge3 *24k*(0,*y*,*z*).

the Czochralski-pulled crystal were used for single-crystal neutron diffraction measurements at 20 K. The data were measured on the SCD instrument at the Intense Pulsed Neutron Source (IPNS), at the Argonne National Laboratory (ANL).[24,25] The data were integrated using *ISAW*, and the absorption correction was carried out with the program *ANVRED*.[26] Structural refinements were done with the Ba6*d* and Ba24*k* models using the program *GSAS*.[27] Selected experimental and crystallographic details are given in Table 4.

Transport Properties. The sample prepared by stoichiometric mixing was ground and pressed by spark plasma sintering methods into a disc. The sample was heated under a pressure of 100 MPa at a rate of 100 °C/min to 865 °C, where it was held for 5 min. A box-shaped sample with dimensions 9.0 × 1.9 × 4.4 mm^3 was cut from the resulting disc. The density was measured to be 4.78 g/cm^3 at room temperature on a home-built device using the Archimedes principle, with water as immersion medium. This is 98.9% of the experimental X-ray density. Table 5 shows the densities extracted both from the X-ray diffraction experiments and as measured by the immersion technique. A crack-free sample was cut directly from the Czochralski-pulled rod with dimensions 9.9 × 1.4 × 1.8 mm^3. The density was found to be 4.92 g/cm^3, which corresponds to 99.4% of the experimental X-ray density. Four copper wires were attached to the samples with silver epoxy. The Seebeck coefficient, electrical resistivity, and thermal conductivity were measured simultaneously in the temperature range 2−300 K, using the thermal transport option (TTO) in a Quantum Design Physical Property Measurement System.

Table 5. Formula Weight Calculated from the Single X-ray Diffraction Model, the Density Based on X-ray Diffraction Data and the Density Measured by Emersion Technique

298 K	$Ba_8Al_{16}Ge_{30}$ Czo	$Ba_8Al_{16}Ge_{30}$ norm	$Ba_8Al_{16}Ge_{30}$ flux
weight (g/mol)	3799	3715	3680
ρ_{X-ray} (g/cm^3)	4.95	4.83	4.78
$\rho_{emersion}$ (g/cm^3)	4.92(6)	4.86(9)	4.81(7)

Results and Discussion

Site Occupancy Factor Rules. The significant difference in scattering contrast between aluminum and germanium compared with gallium and germanium allows for reliable refinement of the host-structure occupancies, even from conventional powder diffraction data. Table 1 shows the refined occupancies from powder X-ray, single-crystal X-ray, and single-crystal neutron diffraction. In the Rietveld powder diffraction refinements, the Ba1 and the host-structure ADPs were constrained to be equal. The absorption correction was adjusted to give ADPs comparable to those obtained from the single-crystal X-ray diffraction data. Even though the powder refinements are less accurate than the single crystal analysis, the results do provide an estimate of how reproduc-

(24) Schultz, A. J. *Trans. Am. Crystallogr. Assoc.* **1993**, *29*, 29−41.
(25) Schultz, A. J.; De Lurgio, P. M.; Hammonds, J. P.; Mikkelson, D. J.; Mikkelson, R. L.; Miller, M. E.; Naday, I.; Peterson, P. F.; Porter, R. R.; Worlton, T. G. *Physica B* **2006**, *385*−*86*, 1059−1061.
(26) Schultz, A. J.; Leung, P. C. W. *Journal De Physique* **1986**, *47*, 137−142.
(27) Larson, A. C.; Dreele, R. B. V. *Los Alamos National Laboratory Report LAUR*, 2004, 86−748.

ible and representative the single-crystal results are with respect to the entire synthesis batch. The $Ba_8Al_{16}Ge_{30}$_czo sample has the 6*c* site close to fully occupied by aluminum, whereas the 24*k* site is almost void of aluminum. The 16*i* site holds about half of the total amount of aluminum in the sample. For $Ba_8Al_{16}Ge_{30}$_norm, the 6*c* site is still the preferred site for aluminum, and the 16*i* and 24*k* sites percentage wise have comparable amounts. For $Ba_8Al_{16}Ge_{30}$_flux, the 6*c* site has almost 50/50% occupancy of aluminum and germanium. In this sample, aluminum tends to avoid the 16*i* site, whereas the 24*k* site holds more than half of the total amount of aluminum in the sample. These trends are independent of the experimental analysis method, and thus the results presumably are representative for the synthesis batch. When comparing the different samples, it is clear that the aluminum content at the 6*c* and 16*i* sites decreases from $Ba_8Al_{16}Ge_{30}$_czo to $Ba_8Al_{16}Ge_{30}$_norm, and it decreases even further for $Ba_8Al_{16}Ge_{30}$_flux. On the other hand, the aluminum content at the 24*k* site increases. The single-crystal diffraction data reveal $Ba_8Al_{16}Ge_{30}$_flux to have the highest aluminum content and $Ba_8Al_{16}Ge_{30}$_czo the lowest.

The site occupancies of aluminum can be rationalized, when considering the bonding environment of the individual host-structure sites. It is well-established that bonds between trivalent elements are energetically unfavorable,[28] and using this simple fact, rules can be established for the maximum trivalent element sof at a given site (sof(III)). In other words, the only premise for the rules is that the host structure will tend to avoid direct III−III bonds. The rules are analogous to the Löwenstein rule known for alumina-substituted silicates, where Al−O−Al bonds are avoided.[29]

Rule 1: 6*c* sof(III) ≤ 100%. There are no direct bonds between two 6*c* sites, part b of Figure 1, and 100% occupancy of trivalent elements can be allowed at the 6*c* site, without causing unfavorable bonds.

Rule 2: 16*i* sof(III) ≤ 50%. The 16*i* site binds to three 24*k* atoms, and one 16*i* atom. Therefore, only up to half of the 16*i* sites can be occupied by trivalent elements, without forming disfavored trivalent−trivalent bonds.

Rule 3: 24*k* sof(III) ≤ 50%. The 24*k* site binds to one 6*c* site, two 16*i* sites, and one 24*k* site. Therefore, only up to half of the 24*k* sites can be simultaneously occupied by trivalent elements.

Rule 4: 6*c* + 24*k* sof(III) ≤ 100%. The 6*c* site binds to four 24*k* sites. Thus, the sum of the trivalent element occupancies at the 6*c* and 24*k* sites should not exceed 100%.

Rule 5: 16*i* + 24*k* sof(III) ≤ 50%. The 16*i* atoms bind to three 24*k* atoms. Thus, at a specific 16*i* site, a maximum of one of the four atoms (16*i* + 3 × 24*k*) can be a trivalent element, that is, 25% local occupancy. However, each 24*k* atom binds to two 16*i* sites, giving a doubling of the allowed combined occupancy.

The refined aluminum site occupancy factors in Table 1 follow the rules remarkably well, considering the simplicity of the argument. Slight violations are observed only for the summed sof's, that is, rules 4 and 5. Table 6 shows refined occupancies for various structures containing trivalent host atoms reported in the literature. The agreement with the sof rules is apparent, and the clathrate structure indeed appears to minimize the number of trivalent bonds. The rules have some interesting consequences, because they limit the amount of trivalent elements that can be contained in the structure. The largest achievable trivalent element content is for a structure with 50% occupancy at the 24*k* and 6*c* sites. This results in a total of 12 + 3 = 15 trivalent atoms in the host structure. Filling the 16*i* by 50% allows a 100% filling at the 6*c* site, but this only sums to 8 + 6 = 14 trivalent atoms in the structure. The avoidance of energetically disfavored trivalent−trivalent bonds drives the stoichiometry in the opposite direction of the Zintl concept. To fulfill the Zintl concept, 16 trivalent atoms are needed per unit cell, but this necessarily will introduce intertrivalent bonds. The structure could instead (i) reduce the valence state of the guest atom or (ii) have vacancies in the host structure. A lower valence state would give a lower electron donation to the host structure, and fewer host-structure atoms would need to be replaced by low valence atoms. The simple sof rules explain, why only few *p*-type trivalent clathrates have been reported in the literature. The introduction of too many trivalent−trivalent bonds simply destabilizes the structure. As an example, attempts to produce *p*-type $Sr_8Ga_{16}Ge_{30}$ have been unsuccesful.[30] Vacancies in the host structure would allow the structure to reduce the number of low valence elements. However, in the constrained occupancy refinements, the presence of vacancies would result in high apparent aluminum content because this would reduce the site scattering power. Additionally, the theoretical densities extracted from X-ray diffraction compare well with the densities found by immersion measurements (Table 5). The refined occupancies and measured densities point to no or low concentrations of vacancies in the host structure.

Table 6. Site Occupancy Factors of Trivalent Clathrate Host Structures Reported in the Literature

	6c (≤100%)	*16i* (≤50%)	*24k* (≤50%)	*6c* + *24k* (≤100%)	*16i* + *24k* (≤50%)
			$Ba_8Ga_{16}Ge_{30}$[8] [a]		
n-type (X−ray)	76	16	37	113	53
p-type (X−ray)	64	17	39	103	56
n-type (neutron)	74	17	37	111	54
p-type (neutron)	60	33	30	90	63
			$Ba_8Ga_{16}Si_{30}$		
Eisenmann[17]	59	8	41	100	49
Bentien[18]	63	11	43	106	54
	61	8	40	101	48
Christensen[32]					
flux	65	8	39	104	47
norm	69	8	36	105	44
czo	69	8	32	101	40
			$Ba_8Al_{16}Ge_{30}$		
Eisenmann[17]	100	60	4	104	64

[a] The *n*- and the *p*-type samples used for X-ray and neutron diffraction studies, respectively, are from the same synthesis batches.

Einstein and Debye Temperatures. The ADPs refined from the diffraction data can give information about the

(28) Blake, N. P.; Bryan, D.; Latturner, S.; Møllnitz, L.; Stucky, G. D.; Metiu, H. *J. Chem. Phys.* **2001**, *114*, 10063−10074.
(29) Löwenstein, W. *Am. Mineral.* **1954**, *39*, 92.
(30) Fujita, I.; Kishimoto, K.; Sato, M.; Anno, H.; Koyanagi, T. *J. Appl. Phys.* **2006**, *99*, 093707.

Table 7. Einstein Temperatures of the Barium Guest Atoms, the Debye Temperature of the Host Structure, and the Disorder Terms[a]

	Ba1 *2a*(U_{iso})		Ba2 *6d*(U_{11})		Ba2 *6d*(U_{22})		Host(U_{iso})		Ba2*24k*(U_{iso})	
	θ_E(K)	d(Å)	θ_E(K)	d(Å)	θ_E(K)	d(Å)	θ_D(K)	d(Å)	θ_E(K)	d(Å)
czo	106(1)	0.029(3)	85(1)	0.053(1)	61(1)	0.077(2)	291(3)	0.022(4)	84(1)	0.052(1)
norm	101(1)	0.037(4)	81(1)	0.043(3)	64(1)	0.173(1)	277(6)	0.030(7)	81(1)	0.068(2)
flux	101 (1)	0.040(3)	85(1)	0.031(6)	69(1)	0.219(1)	293(4)	0.040(3)	83(1)	0.072(2)

[a] Results are Listed for Both the *Ba6d* and *Ba24k* Models.

dynamics of the structure. The host-structure ADPs can be modeled with the Debye expression: where θ_D is the Debye

$$U_{iso}(T) = \frac{3\hbar^2 T}{m k_B \theta_D^2}\left[\frac{T}{\theta_D}\int_0^{\theta_D/T}\frac{x}{\exp(x)-1}\,dx + \frac{\theta_D}{4T}\right] + d^2$$

temperature, m is the average mass of aluminum and germanium, and d^2 describes temperature-independent disorder. The barium guest atoms are assumed to be weakly bonded to the host structure, and these ADPs can be modeled with the Einstein expression: where $\theta_{E,xx}$ is the Einstein

$$U_{xx}(T) = \frac{\hbar^2}{2mk_B\theta_{E,xx}}\coth\left(\frac{\theta_{E,xx}}{2T}\right) + d^2$$

energy along the *xx* direction, m is the mass of barium, and d^2 is a temperature-independent disorder term. Table 7 gives the Debye and Einstein temperatures along with the disorder parameters extracted from fits to the ADPs shown in Figure 2. The tabulated values of θ_E(Ba1) and θ_D are taken from the Ba6*d* model, but the values from the Ba24*k* model are identical within uncertainties. The fractional coordinates of the host-structure atoms only have small variations between the different samples. The cages therefore occupy the same relative amount of the unit cell. The Einstein temperatures in general agree fairly well between the different data sets as a result of the fairly identical slopes observed in Figure 2. The lowest Einstein temperature is observed for the motion in the plane that is parallel to the host-structure hexagon (Ba2 U_{22}). The Einstein temperature is found to increase from 61-(1) to 64(1) and 69(1) K for $Ba_8Al_{16}Ge_{30}$_czo, Ba_8Al_{16}-Ge_{30}_norm, and $Ba_8Al_{16}Ge_{30}$_flux, respectively. This may seem surprising because the unit cell and thereby the cage size is found to increase from $Ba_8Al_{16}Ge_{30}$_czo to Ba_8Al_{16}-Ge_{30}_norm and to $Ba_8Al_{16}Ge_{30}$_flux, giving the guest atom a larger volume to occupy. The increase in Einstein temperature can be interpreted as an increased bonding strength between the barium guest atom and the host structure. In other words, the barium guest atom in $Ba_8Al_{16}Ge_{30}$_flux forms the strongest bond with the host structure. Thus, the Einstein temperature is not just determined by the cage size, but by the details of the chemical interactions between the guest and the host atoms. Distribution changes of aluminum and germanium atoms cause changes in the chemical interactions. This coupling presumably affects how strongly phonons are scattered.

In the Ba24*k* model, the disorder is modeled with off-center positions instead of being absorbed in the ADPs, as in the Ba6*d* model. In this case, the Einstein temperature is fitted to be ~83 K for all of the samples, but for this model it is the distance between the guest atom and the host structure, which gives indications about the bonding strength (below). The Einstein temperature for Ba2 in the related compound $Ba_8Ga_{16}Ge_{30}$ was found by single-crystal X-ray diffraction to be around 60 K for a 6*d*(U_{22}) model and around 82 K using a 24*j*(U_{iso}) model.[8] Thus, overall the Einstein temperature is found to compare well between $Ba_8Al_{16}Ge_{30}$ and $Ba_8Ga_{16}Ge_{30}$, revealing that the potential for the Ba2 guest atom is similar in the two compounds. However, as noted above, there are subtle differences in the Einstein temperature when the host-structure occupancy changes. The Debye temperature for $Ba_8Al_{16}Ge_{30}$ (Table 7) is slightly larger than the value obtained for $Ba_8Ga_{16}Ge_{30}$, where θ_D was found to be ~270 K. The Debye temperature is inversely proportional to the atomic mass, and thus the result reflects the lighter framework of $Ba_8Al_{16}Ge_{30}$ compared with Ba_8-$Ga_{16}Ge_{30}$.

Guest Atom Modeling. Two different approaches have been used for modeling the disorder of the Ba2 guest atom. The Ba6*d* model uses anisotropic ADPs and a disorder parameter, whereas the Ba24*k* model uses noncenter positions and isotropic ADPs to describe the smeared electron/nuclear density of the Ba2 atom. The disorder parameter (d) extracted from the Einstein fit is given in Table 7. In the Ba6*d* model, the disorder is 0.077(2), 0.173(1), and 0.219(1) Å for Ba_8-$Al_{16}Ge_{30}$_czo, $Ba_8Al_{16}Ge_{30}$_norm, and $Ba_8Al_{16}Ge_{30}$_flux, respectively. It should be noted that systematic errors may cause an offset of the ADPs. However, the agreement observed for the disorder parameters of both the host structure and Ba1 between the different samples suggests that the differences observed for Ba2 are genuine. The difference in disorder of the Ba2 U22 is similar to the difference in the unit cell between the different samples; d(norm) − d(czo) = 0.096(2) and d(flux) − d(norm) = 0.046(1) Å compared with a(norm) − a(czo) = 0.100(1) and a(flux) − a(norm) = 0.047(1) Å. The disorder in the U_{11} direction shows the opposite trend compared to U_{22}, where $Ba_8Al_{16}Ge_{30}$_czo has the largest disorder of 0.053(1) followed by d(norm) = 0.043(3), and finally d(flux) = 0.031(6) Å is the lowest value. If the disorder parameters are seen as the principal axes in an ellipsoid, the shape goes from almost spherical (Czochralski-pulled) to an oblate shape (flux-grown).

In the Ba24*k* model, the displacement from the center is refined directly through the additional fractional coordinates ($^1/_4 - x$, $^1/_2$, z). Here, z displaces the guest atom parallel to the hexagon in the host structure, whereas x is a displacement perpendicular to the hexagon. Figure 3 shows the fractional coordinates of x and z, together with a linear fit to the z coordinates. The $Ba_8Al_{16}Ge_{30}$_czo sample has the smallest z displacement from the center of the cage, and the fractional displacement follows the same trend as the disorder parameter in the Einstein fits in the Ba6*d* model. In fact, the refined

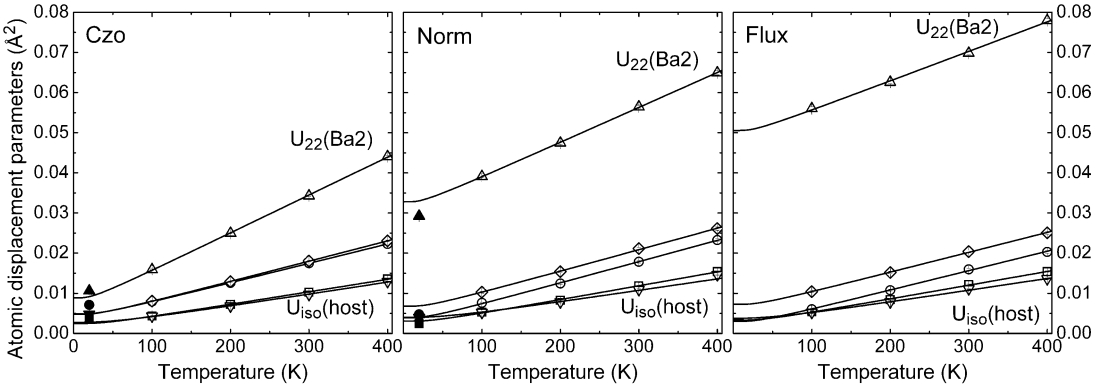

Figure 2. Atomic displacement parameters (ADPs) for three different samples: Czochralski-pulled, conventional synthesis, and flux-grown. The open symbols are the single-crystal X-ray diffraction data, whereas the filled symbols are single-crystal neutron diffraction data. The barium guest atom in the large cage has triangles pointing up and circles to denote the parallel and perpendicular directions, respectively. The barium atom in the small cage is symbolized by squares. The triangles pointing down are the isotropic APDs of the host-structure atoms. The diamonds are the isotropic APDs of the Ba2 guest atom in the Ba24*k* model.

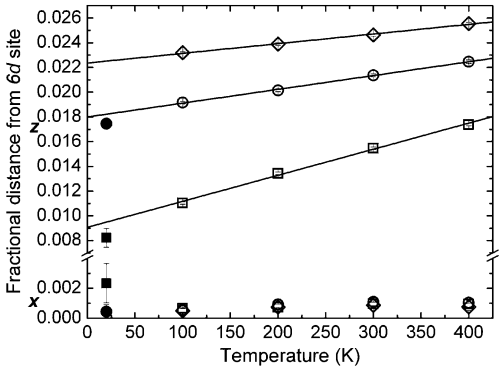

Figure 3. Fractional coordinates of the Ba2 guest atom. The open symbols are single-crystal X-ray diffraction data, and the filled symbols are the 20 K single-crystal neutron diffraction data. The diamonds correspond to the flux-grown sample, the circles to the conventionally synthesized sample, and the squares to the Czochralski-pulled sample.

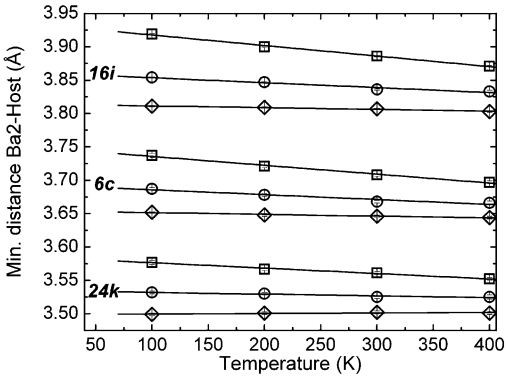

Figure 4. The minimum distance between the three host-structure sites and the Ba2 guest atom (Ba24*k* model). The squares, circles, and diamonds correspond to the Czochralski-pulled, conventionally synthesized, and flux-grown samples, respectively.

distance from the guest atom to the cage center is very similar to the disorder parameter obtained from the Einstein fits. This illustrates that the thermally smeared density of the guest atom can be modeled either as a very large anisotropic ADP or as a combination of disorder and isotropic ADPs. Physically, the latter model is the most correct. Figure 4 shows the shortest distance between the Ba2 atom and each of the host-structure sites 6*c*, 16*i*, and 24*k*. The solid lines are linear fits to the distance. The data reveals that Ba2 in $Ba_8Al_{16}Ge_{30}$_czo moves closer to the host structure at elevated temperatures. Ba2 in $Ba_8Al_{16}Ge_{30}$_norm also has a slight tendency to move closer to the cage wall, whereas the distance in $Ba_8Al_{16}Ge_{30}$_flux appears to be unaltered as function of temperature. This suggests that anharmonic effects are largest in the $Ba_8Al_{16}Ge_{30}$_czo sample, because a change in the equilibrium bonding distance between host and guest with temperature presumably is due to the guest atom moving up in an anharmonic potential. The bonding distance is inversely proportional to the bonding strength. Comparing the distances of the different samples, the $Ba_8Al_{16}Ge_{30}$_czo sample shows the largest distance between the Ba2 and the host-structure atoms, with $Ba_8Al_{16}Ge_{30}$_flux being the smallest. This suggests that the Ba2 guest atom in $Ba_8Al_{16}Ge_{30}$_flux is more strongly bonded to the host structure than in $Ba_8Al_{16}Ge_{30}$_czo. The fitted Einstein temperature supports that the strongest bond is found in $Ba_8Al_{16}Ge_{30}$_flux, whereas the lowest Einstein temperature and thereby the weakest bond is observed for $Ba_8Al_{16}Ge_{30}$_czo. In combination, the analysis shows that the largest anharmonicity is observed for the most weakly bound Ba2 atom, and this is found in the $Ba_8Al_{16}Ge_{30}$_czo sample. The bonding strength presumably is increased as a larger amount of electrons are donated from barium. Thus, barium in $Ba_8Al_{16}Ge_{30}$_flux donates more electrons than in $Ba_8Al_{16}Ge_{30}$_czo and $Ba_8Al_{16}Ge_{30}$_norm, that is, the valence of the barium guest ion increases from $Ba_8Al_{16}Ge_{30}$_czo to $Ba_8Al_{16}Ge_{30}$_flux. The difference in valence is corroborated by the variation in the aluminum content between the different samples. As the aluminum content increases, the barium guest atom is forced to donate a larger number of electrons to the host structure. Thus, the sample with the highest aluminum content also has the highest barium valence ($Ba_8Al_{16}Ge_{30}$_flux).

Neutron Diffraction Data. The values of the refined host-structure germanium/aluminum occupancies from the neutron data are listed in Table 1. The values are in good agreement with the single-crystal X-ray diffraction results. The neutron interacts with the nucleus in the sample, and thus the neutron data provides a description of the nuclear density. The nuclear density of the Ba2 guest atom has a very pronounced difference between $Ba_8Al_{16}Ge_{30}$_czo and $Ba_8Al_{16}Ge_{30}$_norm. In Figure 5, both isosurfaces and contour plots of the Ba2 nuclear density are shown on the basis of the difference

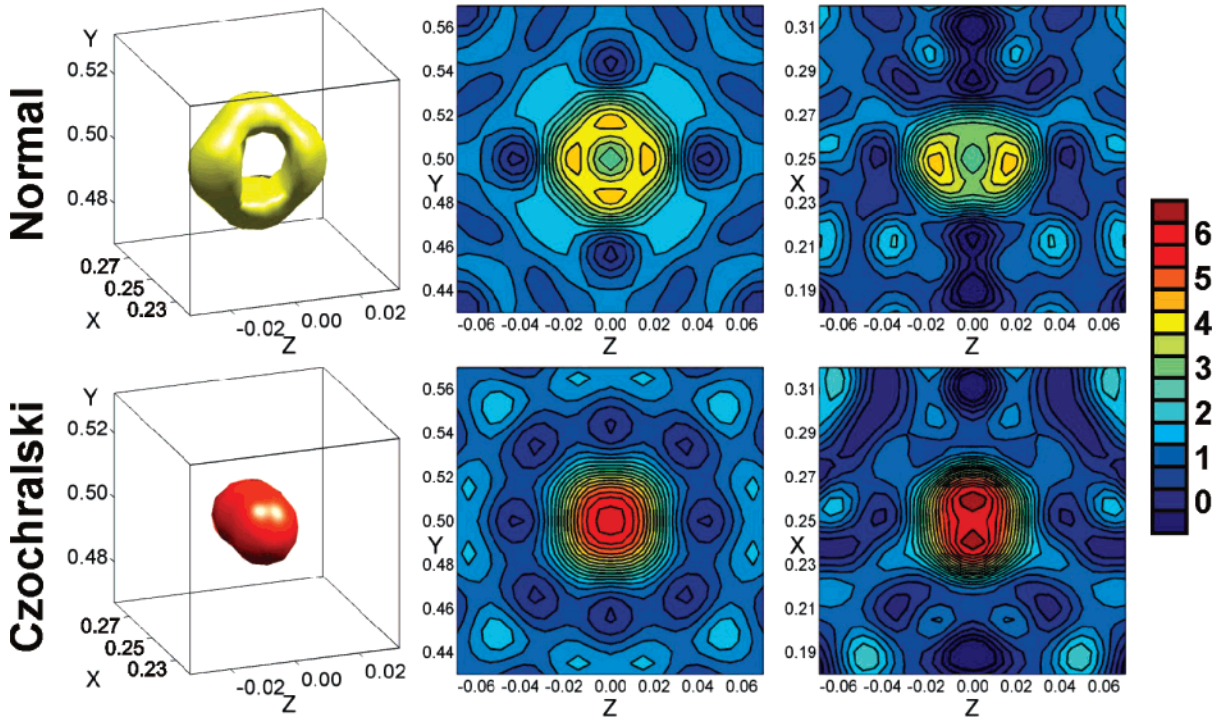

Figure 5. Nuclear density of the Ba2 guest atom obtained from difference Fourier summation with the barium atom removed from the model. The plot on the left is the isosurface of the nuclear density. To the right, contour plots of the nuclear density are shown parallel and perpendicular to the host-structure hexagon.

Fourier density obtained with the Ba2 guest atom removed from the refinements. An elongated shape of the nuclear density is observed for Ba2 in the $Ba_8Al_{16}Ge_{30}$_czo sample, with apparent local maxima pointing toward the hexagons of the host structure. In the $Ba_8Al_{16}Ge_{30}$_norm sample, the Ba2 atom has torus-shaped nuclear density similar to the low-temperature shape found for Ba2 atoms in $Ba_8Ga_{16}Ge_{30}$ and $Ba_8Ga_{16}Si_{30}$.[8,18] It is indeed remarkable that a small change in host structure can have such a significant effect on the guest-atom structure. A local maxima is found at the 24*k* position. In a study of $Ba_8Ga_{16}Ge_{30}$, it was found that the local maxima are in the 24*j* position at 20 K for both the *p*-type and the *n*-type.[8] With increasing temperature, the nuclear density in $Ba_8Ga_{16}Ge_{30}$ changes, and the maxima move from 24*j* to 24*k*. Theoretical calculations on a hypothetical symmetrical cage in $Ba_8Ga_{16}Ge_{30}$ predicted the opposite behavior, with 24*k* maxima at low temperature.[31] Here, levels with 24*j* density get mixed in with increasing temperature. The failure of the theory in reproducing the experimental results presumably lies in the approximation of a symmetrical cage without gallium/germanium disorder. The fact that the $Ba_8Al_{16}Ge_{30}$ structure has 24*k* maxima at 20 K suggests that either the energy scale is different from that of $Ba_8Ga_{16}Ge_{30}$, that is, the 24*k* levels have already been mixed in at 20 K, and thus a nuclear density at very low temperature (<20 K) would have 24*j* maxima or the $Ba_8Al_{16}Ge_{30}$ structure more closely resembles the hypothetical symmetric cage used in the theoretical calculations.

It is noteworthy that, in the case of the $Ba_8Al_{16}Ge_{30}$_czo sample, the Ba2 nuclear density points toward the hexagonal ring of the host structure, where the host-structure 6*c* site is almost fully occupied by aluminum. In this sample, the sof rule is violated for the 6*c* + 24*k* sum (rule 4), and trivalent bonds therefore exist between the 6*c* and 24*k* sites. These bonds are primarily found in the hexagon above and below the guest atom. For the $Ba_8Al_{16}Ge_{30}$_norm sample, the sof rule is violated for the 16*i* + 24*k* sum (rule 5). A significant number of these bonds are found in the equatorial plane of the guest atom. The trivalent bonds represent an electron-depleted area, and it appears that the electron-donating guest atom moves toward the electron-depleted bonds.

The color scale of Figure 5 reveals that the nuclear density for the $Ba_8Al_{16}Ge_{30}$_norm sample is significantly more smeared than for the $Ba_8Al_{16}Ge_{30}$_czo sample. This is in accordance with the larger ADPs refined for the $Ba_8Al_{16}Ge_{30}$_norm sample. The refined ADPs of the Ba6*d* model obtained with the neutron data are shown in Figure 2 as solid symbols. The data agrees fairly well with the single-crystal X-ray diffraction experiment if these values are extrapolated to 20 K. The largest deviation is found for Ba2 6*d*(U_{22}) in the $Ba_8Al_{16}Ge_{30}$_norm sample. The *x* and *z* fractional coordinates obtained with the Ba24*k* model are shown in Figure 3 as solid symbols. The neutron data for the $Ba_8Al_{16}Ge_{30}$_norm sample follows approximately the same behavior as that observed for the X-ray data. However, the $Ba_8Al_{16}Ge_{30}$_czo sample reveals non-negligible displacement in the *x* direction at 20 K, reflecting the significantly different nuclear density observed in this sample at low temperature.

Transport Properties. The lattice thermal conductivity extracted from the total thermal conductivity using the Widemann−Franz Law is shown in Figure 6 for the $Ba_8Al_{16}Ge_{30}$_norm and the $Ba_8Al_{16}Ge_{30}$_czo samples. Both samples show a temperature profile characteristic for con-

(31) Madsen, G. K. H.; Santi, G. *Phys. Rev. B* **2005**, *72*, 220301.
(32) Christensen, M.; Iversen, B. B. Proc. *4th European Conference on Thermoelectrics*; 2006.

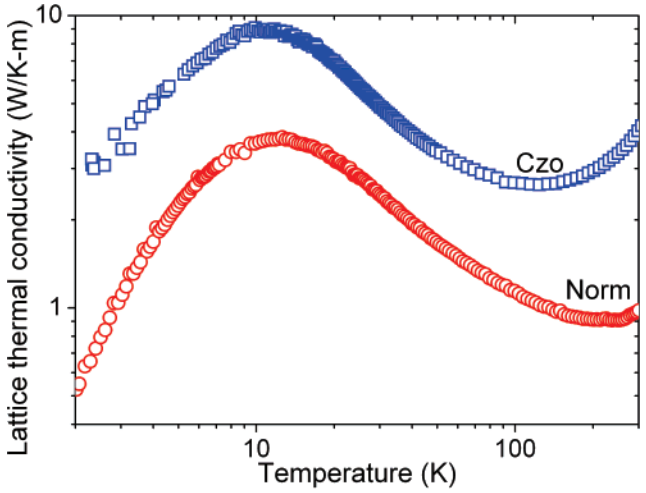

Figure 6. Lattice thermal conductivity for the Czochralski-pulled (squares) and conventionally synthesized samples (circles).

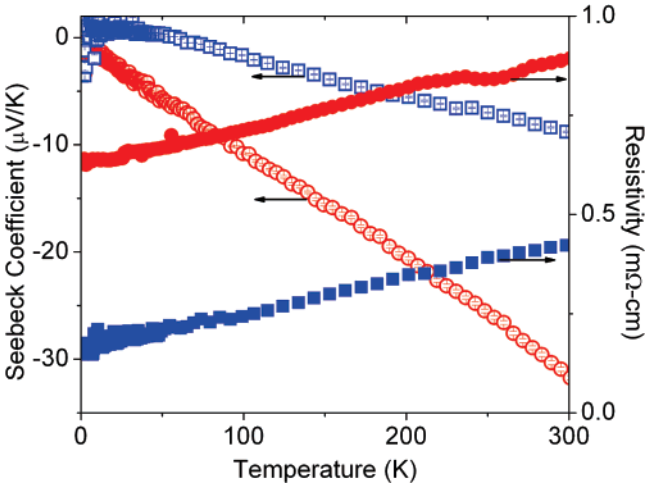

Figure 7. The Seebeck coefficient (open) and the resistivity (solid) for the Czochralski-pulled (blue squares) and the stoichiometric samples (red circles).

ventional crystals with a peak around 12 K. Although the temperature profile is similar for the two samples, the lattice thermal conductivity for $Ba_8Al_{16}Ge_{30}$_czo is a factor of 3 higher than for $Ba_8Al_{16}Ge_{30}$_norm. The higher thermal conductivity for $Ba_8Al_{16}Ge_{30}$_czo can be related to the crystallographic investigations that reveal a weaker-bound guest atom and thereby reduced phonon scattering. The host structure of the $Ba_8Al_{16}Ge_{30}$_czo sample is more ordered than in the $Ba_8Al_{16}Ge_{30}$_norm sample. Thus, additionally, less mass fluctuation scattering can be expected in $Ba_8Al_{16}Ge_{30}$_czo.

The Seebeck coefficient and the resistivity are shown in Figure 7. Both samples are observed to have negative Seebeck coefficients, indicating that the main charge carriers are electrons and that the samples are *n*-type conductors. The Seebeck coefficients are observed to increase linearly for both samples in the measured temperature range from 2 to 300 K. The lower absolute Seebeck coefficient of $Ba_8Al_{16}Ge_{30}$_czo shows that this sample has more metallic character than $Ba_8Al_{16}Ge_{30}$_norm. The resistivity increases with similar slopes for both samples, and the temperature behavior reveals that both samples are metallic. The $Ba_8Al_{16}Ge_{30}$_czo sample has the lowest resistivity, in agreement with the observed Seebeck coefficient (absolute value) for this sample. The transport measurements support the refined occupancies found from the single-crystal diffraction data. Here, the $Ba_8Al_{16}Ge_{30}$_czo sample was found to contain more germanium than the $Ba_8Al_{16}Ge_{30}$_norm sample, and thus more electrons are available as charge carriers. In other words, the $Ba_8Al_{16}Ge_{30}$_czo sample is further away from the Zintl stoichiometry. The higher lattice thermal conductivity for $Ba_8Al_{16}Ge_{30}$_czo is in accordance with the analysis of the multi temperature single-crystal X-ray and neutron diffraction data. The weaker-bonded barium guest atom in the $Ba_8Al_{16}Ge_{30}$_czo sample presumably causes a weaker phonon coupling, and this gives less scattering compared with $Ba_8Al_{16}Ge_{30}$_norm. On the other hand, the $Ba_8Al_{16}Ge_{30}$_norm sample has larger disorder of the barium guest atom (Figure 5), but this does not seem to affect the thermal transport to the same extent.

Conclusion

Site occupancy factor rules have been introduced to explain the host-structure siting of trivalent elements in type I clathrates. It is possible to avoid energetically disfavored bonds between trivalent elements; if the trivalent element sof obey the following rules: Rule 1: $6c$ sof(III) $\leq$ 100%, Rule 2: $16i$ sof(III) $\leq$ 50%, Rule 3: $24k$ sof(III) $\leq$ 50%, Rule 4: $6c + 24k$ sof(III) $\leq$ 100%, Rule 5: $16i + 24k$ sof(III) $\leq$ 50%. The validity of the sof rules were demonstrated for three $Ba_8Al_{16}Ge_{30}$ samples prepared by three different methods. The different synthesis methods, that is, the thermal history, give a clear variation in the aluminum sof's. The changes in host-structure stoichiometry strongly affect the nuclear density of the Ba2 guest atom. The present study provides the first direct demonstration that slight changes in the host-structure stoichiometry can have large effects on the guest-atom structure. From Einstein temperatures and bonding distances, it is concluded that the Ba2 ion forms a stronger bond with the host structure of the flux-grown sample, whereas the Czochralski-pulled sample has the weakest bonding. The bond strength follows the aluminum content, that is, the flux-grown sample has the highest aluminum content, and the Czochralski-pulled sample the lowest. The structure with the weakest bonding shows the most pronounced anharmonic effects on the nuclear potential of the Ba2 guest atom. Disorder parameters of the Ba2 atom obtained from Einstein fits to the ADPs reveal variations in the direction of the disorder. The flux-grown sample has the largest disorder in the plane parallel to the hexagon of the host structure and the smallest disorder perpendicular to this plane. The Czochralski-pulled sample on the other hand has the smallest disorder in the parallel plane and the largest disorder in the perpendicular direction. The nuclear density obtained from 20 K single-crystal neutron diffraction data directly reveals the difference in disorder direction, and the Czochralski-pulled sample shows an elongated shape of the nuclear density, whereas the sample synthesized with conventional methods shows a torus shape. The results demonstrate that the coupling between the host and the guest can be manipulated by subtle chemical changes in the host structure. It is this coupling, which affects the resonance

scattering of phonons in thermoelectric clathrates. The lattice thermal conductivity is a factor of 3 higher in the $Ba_8Al_{16}Ge_{30}$_czo sample than in the $Ba_8Al_{16}Ge_{30}$_norm sample, and this reflects the weaker chemical bonding of the barium guest atom in the Czochralski-pulled sample. The transport properties were found to be in agreement with the crystallographic results, where the sample with the highest refined germanium content was found to have the lowest resistivity and Seebeck coefficient. The key conclusion is that the control of the host-structure chemistry provides a route to manipulate not only the electrical properties but also the thermal conductivity.

Acknowledgment. We gratefully acknowledge the beam time obtained at the Intense Pulsed Neutron Source; Argonne. M. Miller and A. Schultz are thanked for assisting with the data collection. M. Nygren at Stockholm University is thanked for spark plasma sintering one of the samples. The work was supported by DANSCATT.

Supporting Information Available: Results for the refinement of different models against the X-ray powder diffraction data for the three samples, results for the refinement of different models against 100, 200, 300, and 400 K single-crystal X-ray diffraction data for the three samples, results for the refinement of different models against the 20 K neutron diffraction data for the Czochralski-pulled sample and the conventionally synthesized sample, and total thermal conductivity data for these two samples. This material is available free of charge via the Internet at http://pubs.acs.org.

CM071435P